PAPER • OPEN ACCESS

Modeling and prediction of aerodynamic characteristics of free fall rotating wing based on experiments

To cite this article: Mohamed Y. Zakaria *et al* 2019 *IOP Conf. Ser.: Mater. Sci. Eng.* **610** 012098

View the article online for updates and enhancements.

Modeling and prediction of aerodynamic characteristics of free fall rotating wing based on experiments

Mohamed Y. Zakaria[1]**, Carlos R. dos Santos**[2]**, Abdallah Dayhoum**[3]**, Flávio D. Marques**[4] **and Muhammad R. Hajj**[5]

[1] Assistant Professor, acting as department head, Military Technical College, Aerospace Engineering Department, 11766 Cairo, EGYPT

[2] Phd student, Engineering School of São Carlos, University of São Paulo, São Carlos, Brazil

[3] MSc. Student, Military Technical College, Aerospace Engineering Department, 11766 Cairo, EGYPT

[4] Professor, Engineering School of São Carlos, University of São Paulo, São Carlos, Brazil

[5] Professor, Chair of Civil, Environmental and Ocean Engineering, Stevens Institute of technology

E-mail: `zakaria@mtc.edu.eg`

Abstract.   The unsteady vortex lattice method (UVLM) is used to model the aerodynamic loading on different Samara leaves (Maple seed) during their steady state flight. Experiments is performed to verify the analytical results. Parameters including the drop speed, angular velocity and coning angle for different sets of Maple Samaras were determined from experiments. The aerodynamic loads were calculated using UVLM against the forces required for maintaining a steady state flight as obtained from the experiment. Consequently, the UVLM approach yields adequate aerodynamic modelling features that can be used for more accurate flight stability analysis of the Samara flight or of decelerator devices inspired by such flight.

1. Introduction

Deployment of critical and valuable payloads can be delivered accurately on target and with a controllable approach. There has been a flurry in unsteady aerodynamic lifting mechanisms based on inspiration of birds and insects watching [1, 2]. These new mechanisms extended to be essential for micro aerial vehicles design process based on unsteady aerodynamics and non-conventional lifting mechanisms (e.g Leading edge vortex (LEV) [3, 4], Clap and Fling mechanism, Dynamic stall, etc...). Of particular interest is the maple seed self rotating mechanism. Maple samaras consist of an enclosed seed (enclosed concentrated mass) and a single wing with different shapes that is carried by the wind over a long distances. The wing can attain a terminal velocity in a gust or still air before reaching the ground. Because the enclosed seed constitutes a concentrated mass, the maple samara wing always reorients itself during falling through the air such that the enclosed seed is positioned below the wing for pressure stability. The falling velocity along with the wing shape generates aerodynamic loads on the wing, consequently force the wing to spin around a vertical axis [5].

Birds and insects sometimes use steady aerodynamics as a flight mode (Gliding or soaring) that achieves a low energy consumption. In gliding mode, bird's descend speed is directly proportional to the aspect ratio. Another form of gliding with rotating wing is the maple seed gliding (autorotation). Spinning wings have raised the interest in powered and gliding flight [6]. The decelerating properties of single-winged have also inspired the design of precision airdrop devices [7], because of their stability and steady terminal velocity during descent.

Samara-type decelerators have also been proposed as sensor-fused submunitions capable of scanning a target area as it spins downwards after being deployed [8, 9, 10, 11]. Such decelerators can also be used for distributed sensing, particularly for environmental monitoring tasks using aerial deployment of rotary micro aeriel vehicles [12]. Single-winged micro aerial vehicles (MAVs) can be suitable when high maneuverability missions with hovering capabilities are required. As powered aerial vehicles, samara-type MAVs, also called monocopters, can be designed in different kinematic forms to provide the necessary spinning moment around the vehicle center of gravity. The mono-wing rotorcraft called SAMARAI from Lockheed Martin with a span

of approximately 6 cm and a weight of 10 grams is an example of self-propelled samara-type MAV [13, 14]. Figure 1 shows previous trials for mimicking and testing such articles to exploit the autorotation feature found in the samara.

| (a) | (b) | (c) | (d) |
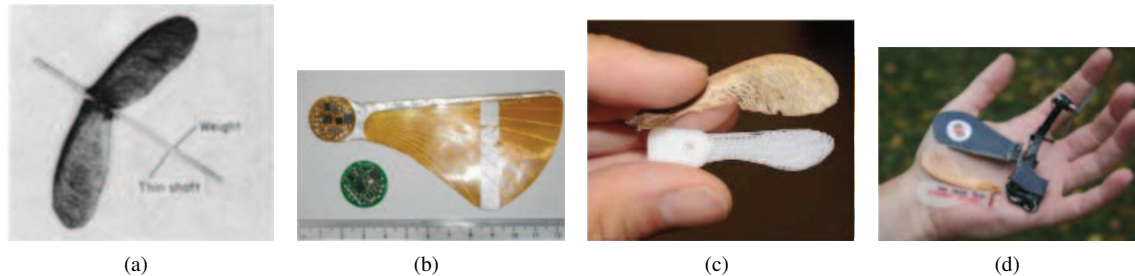
Figure 1. Previous experimental and fabrication attempts for samara.

Experimental measurements have provided significant information for the flight performance of samara wings. Typical experiments have included sequential imaging of the samara wing during its free fall or by using wind tunnel testing and Particle Imaging Velocimetry[15, 16, 17, 15, 18, 19, 20, 21]. These trials stemmed from the need to explore the flow characteristics around falling wings at different regimes.

Single-winged samaras flight has shown three motion regimes when falling in still air (no gust or side wind). In the first regime, the motion is irregular and mostly controlled by gravitational acceleration. In the second regime, the balance between the asymmetric mass distribution and the aerodynamic forces induces a helical motion. Finally, after assuming a proper alignment, the aerodynamic thrust component (in the vertical direction) balances the weight of the samara leading to a steady descend velocity. The air flowing around the rotating seed generates rotation, which in turn, generates thrust. Thrust can also be obtained with propellers set offset from the center of gravity of the vehicle [22, 23, 24]. It has been recently observed that during the wing rotation, a compact stable leading edge vortex emanated resulting in a total lift enhancement. This LEV mechanism allows the samara wing to drop at a lower speed than non-spinning seeds [3, 25].

There is a natural connection between spinning flight of samara wings and helicopter aerodynamics (autorotation mode). Early single-winged samara aerodynamic models are based on the blade element momentum theory (BEM). This method based on calculating the cross-sectional relative velocities then integrating the sectional aerodynamic forces and moments along the wing span and assuming uni-directional variation of induced velocities through the rotating disc plane of rotation [5, 15, 26, 27]. Despite its simplifications, the BEM theory has provided a good understanding of the flight physics of samara wings [20, 28, 29]. Yet, one of the salient limitation of using BEM is that it does not capture the fully localized unsteady effects and the wake influence on the total general forces. In addition, the solution obtained based on BEM is very sensitive to the kinematic input parameters to run the simulation.

On the other hand, high-fidelity computational aerodynamic models based on solving the Navier-Stokes equations may not be practical for predicting the critical kinematics and aerodynamics parameters which controls the overall performance of the such wings. Nonetheless, the treatment of the basic fluid mechanics equations are essential to explore important mechanisms of fluid-structure interaction during spinning flight [30].

An alternative formulation that has been used to determine aerodynamic loads is the unsteady vortex lattice method [31]. This panel method uses a closed formulation of vortices and after imposing Biot-Savart law to calculate discrete circulation in a quadrilateral mesh panels of the wing surface. In the unsteady version of this method, the wake effects are also included to an extent of te cords downstream, thereby accounts for dynamic delay in the aerodynamic loading. Despite the limitation of this method compared to potential flow behavior, local gradients of the circulation can be calculated, yielding more accurate distributed loads.

In this work, experiments were performed to identify the basic kinematic parameters (falling speed, V_{ter}, angular speed ω, and conning angle, γ). The output of the conducted experiments is taken as an input parameters for modeling the unsteady aerodynamics on single-winged samara using unsteady vortex lattice method (UVLM). For a collection of samara wings, three sets are categorized are based on their morphologies and other features such as aspect ratio, AR and leading edge curvatures. A nondimenstional relations obtained to relate the physical interpretations for the wings motion and constraints of such single rotating wings.

2. Experimental setup

Experiments were performed by using a designed test-rig consists of a mechanism holds two PHOTRON ultima APX-RS high CCD cameras with a frame rate of 250, a maximum resolution of 1024x1024. A 1m x 1m white board placed on the ground at which a grid is drawn and discretized by square lines of of area 10 cm x 10 cm. The camera is used to capture the motion (the dispention rate from the drop position and angular velocity) from a top view of the samara fall (fixed above the board center by 1m). The other camera is fixed from the side (apart from the board central vertical axis by 1m) to capture the wing's vertical trajectory during its fall and the coning angle. Figure 2 shows a schematic of the designed test-rig layout illustrating the two recording plans. The experimental tests includes recorded videos for various shapes samara wings based on a free toss (the wing is placed at a horizontal position). Each samara wing is tossed three times retaining the initial drop conditions. Using the recorded data for each wing set, an image frames were obtained to explore the main features that characterize samara flight.
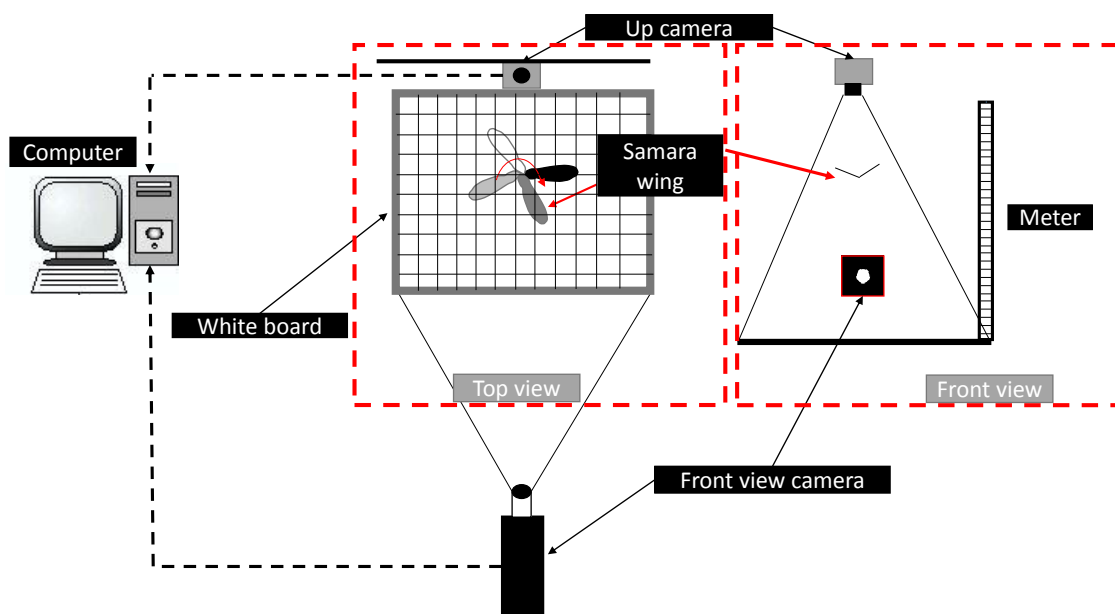

Figure 2. Experimental setup layout for measuring the kinematics of the samara wings.

Figure 3 shows the selected planforms of the samara wings that were used in this investigation. The samples from (1 to 5) as labelled in Figure 3 are characterized by a straight leading edge. Sample wings from (6 to 10) have a curved leading and trailing edge. All tested samara wings exhibited remarkable stability during their descend within three characteristic regimes. Figure 4 shows a sequence of captured frames for typical flight regimes identified from 20 frames of samara wing type labeled number 9 (*cf.* Figure 3) initiated by a random toss. In the first regime, (frames 1-4 in Figure 4), fast variations in the pitch and conning angles of the single-wing are observed. The second regime (frames 5–12 in Figure 4) is characterized by a helical path whereby the samara rotates about a vertical axis. The samara reaches a steady-state rotation and constant downward (terminal) velocity in the third regime (frames 13–20 in Figure 4). In the steady state, the samara rotates about the vertical axis either in a clockwise or counter-clockwise direction depending on the initial drop condition. The tilt and the pitch of the wing remains more or less constant, and to a good approximation, the samara falls along a helical path. Also, for the case of samara 9, a constant conning angle of about 35 degrees is observed in this regime. The same pattern was observed for the other tested samara wings including the three stage flight pattern. However, some wings differ in their transition time from one stage to another, as well as the rotational direction, velocities, and conning angles. Measurements of the relevant flight parameters is extracted from the recorded frames. Figure 5 illustrates the notation used to represent the geometric and kinematic parameters of the tested samaras.

Figure 3. Maple samara samples.
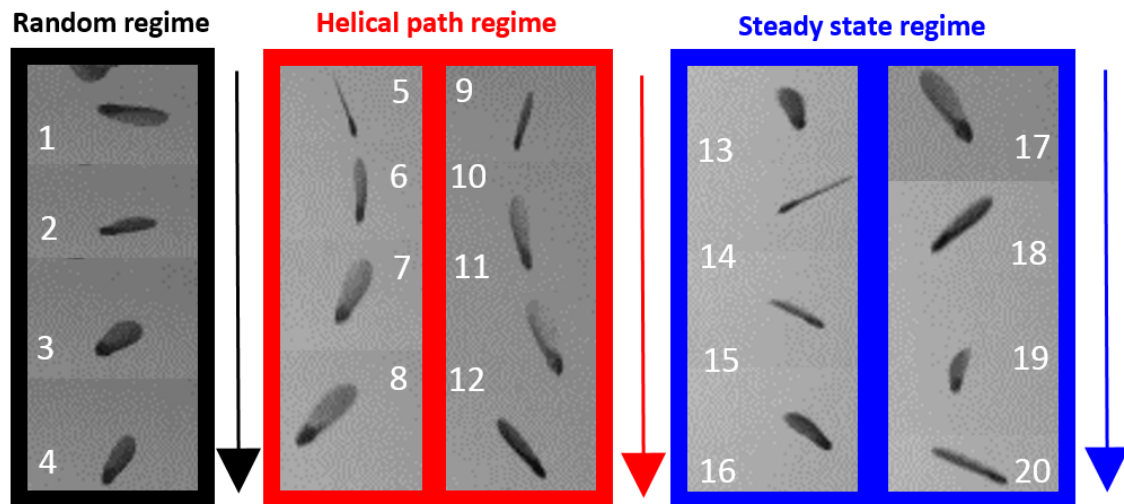
Figure 4. Free falling sequence with the transitional flight regimes.
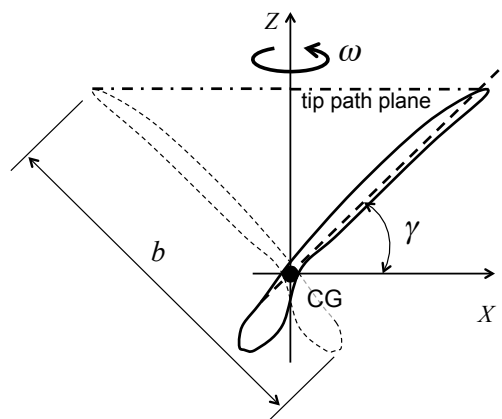
Figure 5. Maple samara geometric and kinematic parameters.

2.1. Prediction of kinematic parameters

Table 1 summarizes the results extracted after post processing and analysis of the obtained data (rotational speed ω, the terminal descent velocity V_{term} and the conning angle γ at the steady-state descent flight) along

with a basic parameters such as mass m, samara span b, area S and the mean aerodynamic chord $\bar{c}$ of the samara wings.

Table 1. Maple samaras geometry information and performance during falling.

Samara	m (mg)	b (mm)	S (mm^2)	$\bar{c}$ (mm)	ω (rad/s)	V_{term} (m/s)	γ (deg)
1	134.1	42.4	448.9	11.3	116	1.060	12.2
2	78.9	37.1	300.0	8.48	124	1.215	14.5
3	64.1	34.7	274.0	8.31	116	1.250	5.5
4	41.1	29.1	200.1	7.25	141	0.962	25.6
5	58.0	25.0	159.5	6.98	242	1.192	11.3
6	181.0	62.6	592.0	10.0	113	0.886	9.8
7	169.9	60.9	643.6	12.1	116	1.012	13.8
8	122.2	49.0	364.6	8.15	104	0.940	7.8
9	13.2	25.2	169.4	7.30	97	0.500	35.2
10	12.8	24.6	136.6	5.96	111	0.534	33.3

Closer observations to the wings shapes (*cf.* Figure 3) and steady-state flight performance (*cf.* Table 1) allows for classifying these samaras into three sets. The first set with samaras 1 to 5 is characterized by a straight leading edge. The second set comprises samaras 6 to 8 and is characterized by a non straight leading edge and relatively high mass values. The third set includes samaras 9 and 10 and is characterized by a relatively small mass and non straight leading edge. The descent velocity for all sets of samaras are shown in Figures 6(a) to 6(c). This velocity was measured from the obtained data and encountered all flight regimes (*cf.* Figure 4). The first segment in time for all samaras falling velocities follow a free-fall pattern with an acceleration that is close to the gravitational acceleration. The transitional motion (helical path) towards constant terminal velocity comprises deceleration caused by aerodynamic drag effects. More significant variations in the deceleration phase are observed in set 1 than in sets 2 and 3. Furthermore, maple samaras from set 3, which have almost 1/10 the mass of the samaras in set 2, have a terminal velocity that is half of the terminal velocity of sets 1 and 2. It is also important to consider that the conning angle observed in this set is much larger than the ones observed in sets 1 and 2.

2.2. Prediction of non-dimensional parameters

In order to simplify and parametrize relations, nondimenstionalization is used by removing all units from an equation involving physical quantities by a reasonable substitution of related variables. First, the geometric parameters of the samara seed is shown in Figure 7 to assign some variables responsible for generating the required thrust force in autorotation mode.

The rotating wings thrust will be evidently dependant on the speed of descend V_{ter}, specific mass of the air, ρ, on the number of revolution n and wing diameter D. The output thrust due to wing's motion is a function of some variables can be written as:

$$T = f(V_{ter}^x \rho^y n^z D^w) \tag{1}$$

In order to calculate the exponents, we replace all the members with respective units and dimensions as follows:

$$[kg]^1[m]^0[s]^0 = [ms^{-1}]^x[kgs^2m^{-4}]^y[s^{-1}]^z[m]^w \tag{2}$$

after arrangement, we have:

$$[kg]^1[m]^0[s]^0 = [kg]^y[m]^{x-4y+w}[s]^{2y-x-z} \tag{3}$$

In order that the dimensions on both sides of the equation is equal, also the indices of receptive basis must be equal,

$$1 = y, \;\; 0 = x - 4y + w, \;\; 0 = 2y - x - z \tag{4}$$
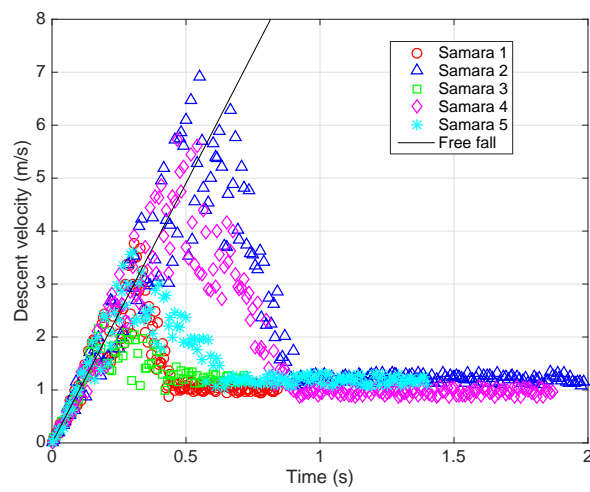
(a) Samaras 1 to 5

(b) Samaras 6 to 8

(c) Samaras 9 and 10

Figure 6. Terminal velocities for all samaras.

Figure 7. Maple samara geometric and kinematic parameters.
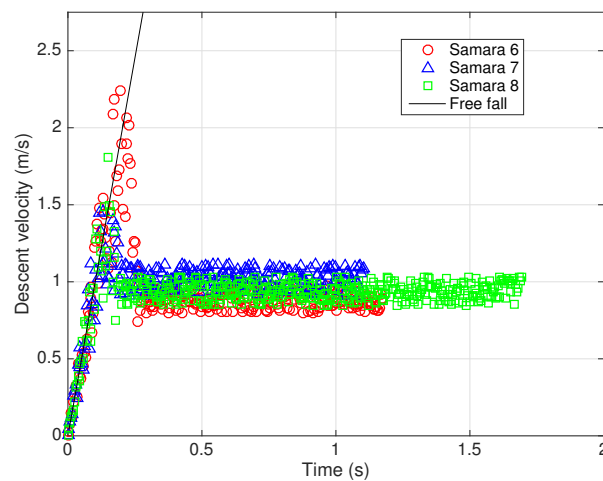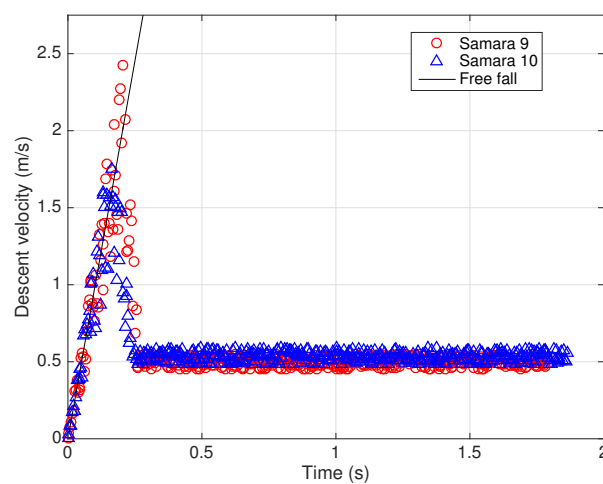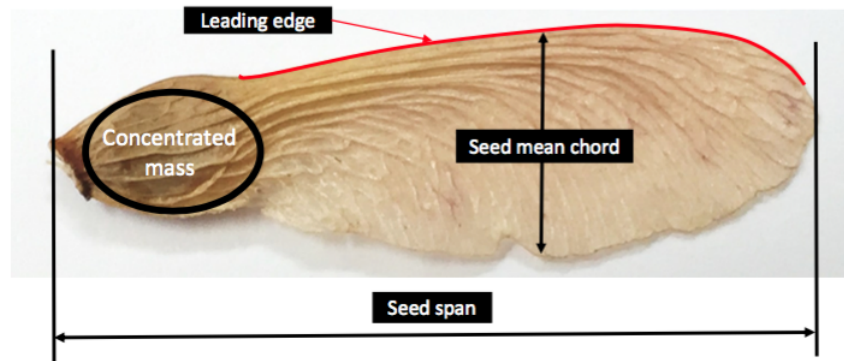
After substitution into eq. 14, we have:

$$T = \left(\frac{V_{ter}}{nD}\right)^x \rho n^2 D^4 \qquad (5)$$

Advance ratio is a non-dimensional parameter, it introduces proportionality only. The index remains unknown but the thrust coefficient $\overline{\alpha}$ can be determined experimentally using wind tunnel.

$$\overline{\alpha} = \frac{T}{\rho n^2 D^4} \qquad (6)$$

More analysis can be conducted by introducing the Reynolds number from two different perspectives. The first, based on the rotational speed of the samara wing named as $Re_1 = 0.75\,\rho\,\bar{c}\,\omega\,b\cos\gamma/\mu$ and the second, based on the terminal descent velocity as $Re_2 = \rho\,c\,V_{term}/\mu$. Table 2 show the values of the Reynolds number calculated by these two definitions for the samara wings . The well known dimensionless parameter can be obtained by dividing the two calculated Reynolds numbers which known as dimensionless velocity ($V_{ter}/R\omega$). This parameter is a very important descriptive ratio to show to some extent the loading constraints for such wing according to the gravitational force, in fixed wings we can relate this ratio to a glide ratio.

Table 2. Samaras Reynolds Number

Samara	Re_1	Re_2	Re_1/Re_2	wing loading (mg/mm^2)	σ
1	2023	849	2.4	0.298	0.079482
2	1311	705	1.9	0.263	0.06938
3	1168	683	1.7	0.233	0.072434
4	927	465	2.0	0.205	0.075216
5	1449	561	2.6	0.363	0.081233
6	2883	600	4.8	0.305	0.04806
7	2782	737	3.8	0.263	0.055237
8	1576	536	2.9	0.335	0.048911
9	506	228	2.2	0.077	0.084911
10	538	216	2.5	0.093	0.071851

The mean value for the relation between Re_1 and Re_2 is 2.67 with a standard deviation of 0.96, which indicates that samaras tend to an optimal relation between rotational and descent velocities.

3. Analysis based on momentum theory
According to Azuma and Yasuda [15] and Gessow and Myers [32], the momentum theory and the blade element theory yield good estimates of the aerodynamic force coefficients for samaras. First, the thrust force (T) during the steady state flight is balanced by the weight of the seed, *i.e.*, $T = mg$, or:

$$C_T = \frac{mg}{\rho A (R\omega)^2} , \qquad (7)$$

where A is the rotating disk area, ρ denotes the air density, and R is an equivalent radius taken at the samara tip rotating path. Denoting the induced velocity by v, the momentum balance yields:

$$T = 2\rho A(V_{term} - v)v \ . \tag{8}$$

Optimal operation is attained when $\frac{\partial T}{\partial v} = 0$, or $v = V_{term}/2$, which yields:

$$V_{term} = \sqrt{\frac{2T}{\rho A}} = \sqrt{\frac{2mg}{\rho A}} = \sqrt{2C_T(R\omega)^2} \ , \tag{9}$$

or

$$\frac{V_{term}}{R\omega} = \sqrt{2C_T} \ . \tag{10}$$

This equation shows that the terminal velocity, which is a measure of the performance of auto-rotational flight, is proportional to the square root of the disk loading if the rotor is operating in its optimal state.

Another measure related to the performance of the auto-rotational flight is the tip speed ratio defined by $V_{term}/(R\omega)$, which is related to the drag coefficient C_D multiplied by the solidity $\sigma = S/A$ (ratio between the samara and disk areas). This relation is based on the power (or torque) resulting from the drag of the rotary wing and the power (or driving torque) generated by the vertical descent of the thrusting rotor and is given by:

$$\frac{V_{term}}{R\omega} = \left(\frac{\sigma C_D}{2}\right)^{1/3} \ , \tag{11}$$

Which concludes that the tip speed ratio is proportional to the cubic root of the equivalent profile drag coefficient σC_D.

By considering that the thrust over the solidity C_T/σ is also a measure of the mean lift coefficient, C_L, Gessow and Myers [32] concluded the following relation

$$\frac{C_T}{\sigma} = \frac{1}{6}C_L \ . \tag{12}$$

Azuma and Yasuda [15] stated that the constant$(1/6)$ is not reliable and is thought to be larger than the actual value. Table 3 presents calculated thrust coefficient C_T, drag coefficient C_D and lift coefficient C_L as obtained from the data presented in Tables 1 and 4. The results show that thrust coefficient for samaras 1-5 (set 1) varies between 0.03 and 0.08. These values are larger than values of thrust coefficients for samaras 6-8 (set 2) that vary between 0.012 and 0.026 and the smallest samaras 9 and 10 (set 3) that have thrust coefficients about 0.04. The same differences can be seen in drag coefficients with samaras of set 1 having the largest values, between 0.3 and 1, and samaras of set 2 having the smallest values, between 0.1 and 0.3. Of particular importance, however, is the ratio of C_L/C_D, which seems to be more or less constant with a value of approximately 4 for set 1, varies between 6 and 10 for set 2 and admits values around 5.5 for the two samaras of the last set.

Table 3. Momentum theory aerodynamic coefficients estimation

Samara	C_T	σC_D	C_D	C_L	C_L/C_D
1	0.05100	0.06500	0.3800	1.8000	4.6900
2	0.07600	0.11800	0.8500	3.2500	3.8500
3	0.07100	0.10600	0.9700	3.8500	3.9900
4	0.05900	0.08000	0.6200	2.7000	4.3800
5	0.03300	0.03400	0.2600	1.5300	5.8200
6	0.01200	0.00700	0.1100	1.0300	9.6800
7	0.01600	0.01200	0.1500	1.2100	8.3400
8	0.02600	0.02300	0.3300	2.2100	6.6100
9	0.04100	0.04800	0.4300	2.2600	5.2100
10	0.03600	0.03900	0.4300	2.4100	5.5800

4. Analysis via unsteady aerodynamic modeling

The Unsteady Vortex Lattice Method (UVLM) divides the lifting surface into panels. A vortex ring is then associated with each of these panels. Its center is set at the 3/4 of the panel chord length and extends between $1/4$ of the panel chord length and $1/4$ of panel chord length after the panel end. One collocation point is set in each panel in the middle of the vortex ring and its normal vector is calculated in this point. In a lifting surface with $i = 1, 2, ..., M$ panels in the chord direction and $j = 1, 2, ..., N$ panels in span direction, a counter $K = 1,$ $2, ..., M \times N$ is used to define the number of each panel.

The velocity induced by all the vortex rings, including those that have shed from the wake, is calculated at each control point and the non-penetrability condition is applied in order to get the intensity of each vortex ring in the lifting surface, according to the linear system,

$$\begin{pmatrix} a_{1,1} & a_{1,2} & ... & a_{1,MN} \\ a_{2,1} & a_{2,2} & ... & a_{2,MN} \\ \vdots & \vdots & \ddots & \vdots \\ a_{MN,1} & a_{MN,2} & ... & a_{MN,MN} \end{pmatrix} \begin{Bmatrix} \Gamma_1 \\ \Gamma_2 \\ \vdots \\ \Gamma_{MN} \end{Bmatrix} = \begin{Bmatrix} RHS_1 \\ RHS_2 \\ \vdots \\ RHS_{MN} \end{Bmatrix} \ , \tag{13}$$

where a_{K_1,K_2} is the influence coefficient from the vortex ring K_2 at the control point K_1 and it is equal to the normal velocity that the vortex ring induces at the control point if it had circulation $\Gamma_{K_2} = 1$. Each element on the right hand side is $RHS_K = -(\vec{v} + \vec{v}_w)_K \cdot \vec{n}_K$, where $\vec{v}$ is the wind flow velocity relative to the surface and $\vec{v}_w$ the velocity induced at the control point K by all the others vortex rings in the wake created before the instant t.

In order to satisfy the Kutta condition, the wake is created at each instant of time at the trailing edge by shedding a new vortex line that has an intensity equal to that of the panel along the trailing edge. At the next time step, the wake vortex ring is closed with the points of the wake generated at that instant. At each instant of time all the points in the wake generated in previous steps are modified following the induced velocity generated by all the vortex rings on the surface and in the wake.

Unsteady aerodynamic loads can be calculated from the circulation Γ_K of the Kth panel and the respective influence of the wake circulation [31]. Using the unsteady Bernoulli equation, the unsteady pressure difference on the Kth panel is given by,

$$\left(\frac{p_l - p_u}{\rho} \right)_K = \left(\frac{\Delta p}{\rho} \right)_K = \left(\frac{V_u^2 - V_l^2}{2} \right)_K + \left(\frac{\partial \phi_u}{\partial t} \right)_K - \left(\frac{\partial \phi_l}{\partial t} \right)_K \ , \tag{14}$$

where p denotes the static pressure, V is the tangent velocity, ϕ is the velocity potential, and the subscripts u and l are used to represent the upper and lower surfaces, respectively.

From the definition of circulation,

$$\left(\frac{\partial \phi_u}{\partial t} \right)_K - \left(\frac{\partial \phi_l}{\partial t} \right)_K = \frac{\partial \Gamma_{i,j}}{\partial t} = \frac{\Gamma_{i,j}(t) - \Gamma_{i,j}(t-1)}{\Delta t} \ , \tag{15}$$

for $i = 1, 2, ..., M$ and $j = 1, 2, ..., N$, and by observing the Kutta-Joukowski theorem, the normal force on each panel is obtained from:

$$\vec{F}_{N_K} = -\left(\Delta p \Delta S \right)_{i,j} \vec{n}_{i,j} \ , \tag{16}$$

where ΔS is the area of each panel.

5. Results and discussion

The aerodynamic load distribution on each samara under investigation was computed with the UVLM. Figure 8(a) depicts an example of a panel mesh for samara 8, in which the number of discrete panels were 20 in the span direction ($N = 20$) and 10 in the chordwise direction ($M = 10$). Time simulations were performed for prescribed rotations around the estimated center of gravity for each samara using parameters from the steady-state flight characteristic observed experimentally. Mesh refinement tests were also executed, revealing that the aforementioned values for $N \times M$ panels correspond to an adequate computational cost-benefit trend. A fixed time step of 10^{-3} seconds was used, based on the convergence of simulations from smaller to larger sampling rates. Figure 8(b) shows a perspective of the spatial shape for the shedding wake.

The aerodynamic simulations of the steady-state flight of the samaras depend on the spanwise angle of attack distribution during rotational motion, influenced by the pitch angle at the rotation axis. The pitch angle parameter is different for each of the samaras due to their own morphologies, as well as their mass distribution.

(a) Samara 8 panel mesh   (b) Wake
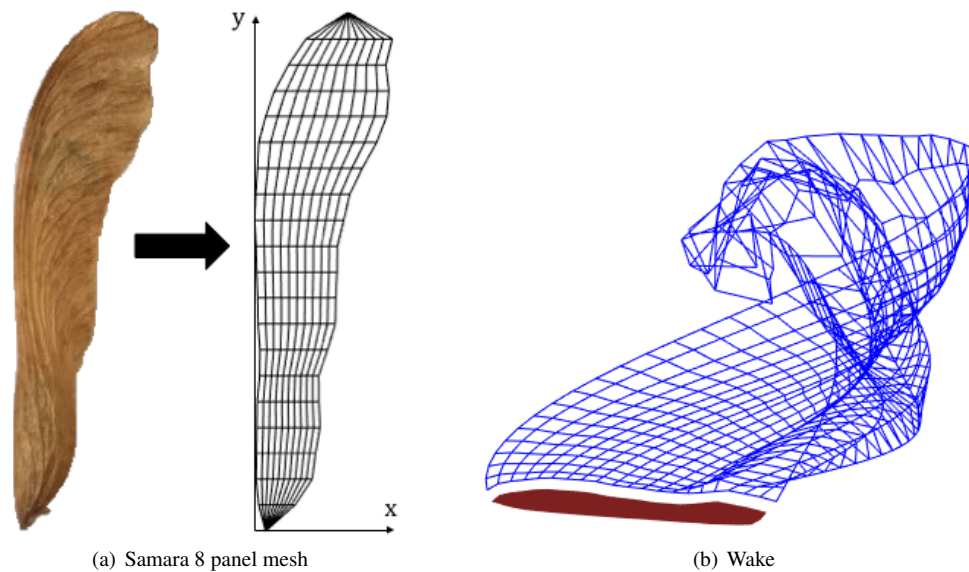
Figure 8. UVLM mesh example and a wake from a typical simulation.

Table 4. Pitch angle per samara estimation.

| Samara	Weight (mN)	Pitch Angle Interval (deg)	Vertical Force Interval (mN)	$\frac{x_{CG}}{b}$
1	1.316	[0.0 2.0]	[1.272 1.350]	0.31
2	0.774	[-21.0 -19.0]	[0.759 0.798]	0.30
3	0.629	[-17.0 -16.0]	[0.610 0.636]	0.17
4	0.403	[-5.0 -2.0]	[0.390 0.416]	0.24
5	0.569	[7.0 10.0]	[0.554 0.582]	0.22
6	1.776	[10.5 12.0]	[1.722 1.822]	0.18
7	1.667	[2.0 3.5]	[1.612 1.703]	0.18
8	1.199	[11.0 13.0]	[1.174 1.240]	0.18
9	0.129	[17.0 19.0]	[0.126 0.134]	0.13
10	0.126	[21.0 23.0]	[0.124 0.128]	0.13

The assessment of the pitch angle of each specimen was based on observing the flight path and extracting the attitude of that specimen along its rotational motion against the freestream. The superior and inferior values of the pitch angle used in the simulations and respective vertical forces are summarized in Table 4. The criterion to determine the pitch angle range is that computed vertical force during steady-state flight should not vary more than $\pm 3.5\%$ from each the samara weight. Because no geometric twist is considered in the model, pitch angles were considered as constant along the samara span. The centers of gravity positions ($\frac{x_{CG}}{b}$) used for each case were based on observations of the samara flight path and are shown in Table 4, where the errors are estimated to be between $\pm 5\%$.

Figures 9 to 11 show the aerodynamic loading in terms of the vertical and horizontal force components distributions for the steady-state condition per samara in their respective set. For set 1 (*cf.* Figure 9), where the samaras have a straight leading edge along the span direction, the contour plots show an intense suction area near the leading edge and mostly close to the rotation axis. Except for samaras 1 and 5, the larger suction is shifted towards the tip, which differentiates the flight performance of these specimen in relation to the other from the set 1. It is interesting to note here that the overall lift coefficient from the experimental measurements calculated with the momentum theory (*cf.* Table 3) was less than 2 for samaras 1 and 5 and larger than 2.5 for samaras 2, 3 and 4.

For set 2, which includes the samaras that have significant curved leading edges, the plots show strong suction peaks towards the leading edge near the tip, as depicted in Figure 10. This set of samaras has relatively low lift coefficient (less than 2.5, *cf.* Table 3). One could note that the suction peak near the leading edge extends more towards the tip as the curvature of the leading edge is increased. The long span and high capacity

for generating lift at the samara tip are in agreement with the observation that they have relatively large tip velocities. Moreover, the experiments have demonstrated that the samaras of this set expend lesser time in the helical transition. The aerodynamic simulations can be used to infer that the reason for quick transition to steady-state path is due to strong lift towards the leading edge near the tip.

The samaras of set 3 are the lightest and smallest ones. Figure 11 also exhibits the presence of suction peaks near the leading edges, but mostly at the mid-span position. Although the lift coefficient is between those of straight and curved leading edges, the relatively large horizontal force and small span cause its tip velocity to be small. This results in the worst descent performance among all sets.

(a) Samara 1

(b) Samara 2

(c) Samara 3
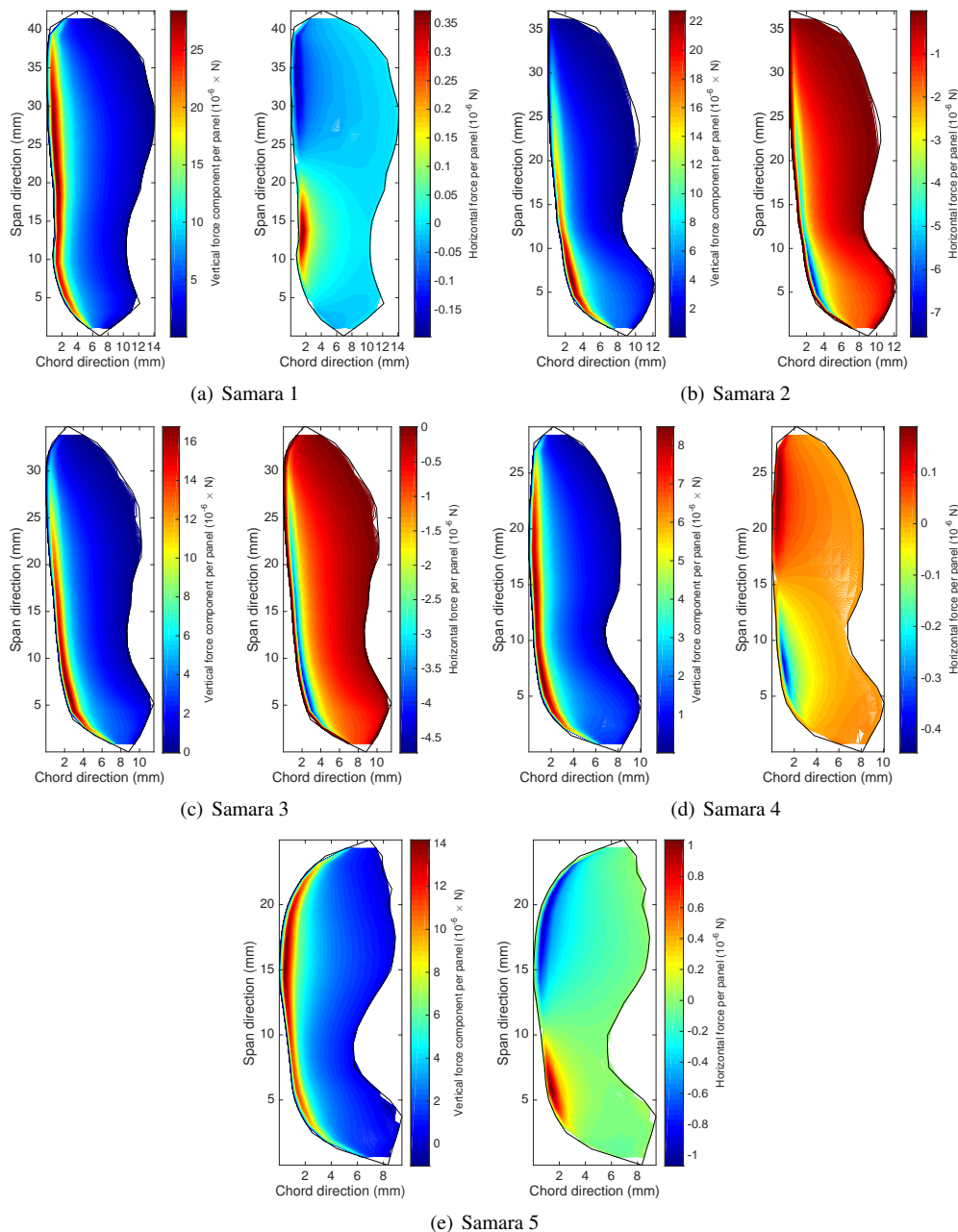
(d) Samara 4

(e) Samara 5

Figure 9. Vertical and horizontal aerodynamic forces per samara – set 1.

(a) Samara 6
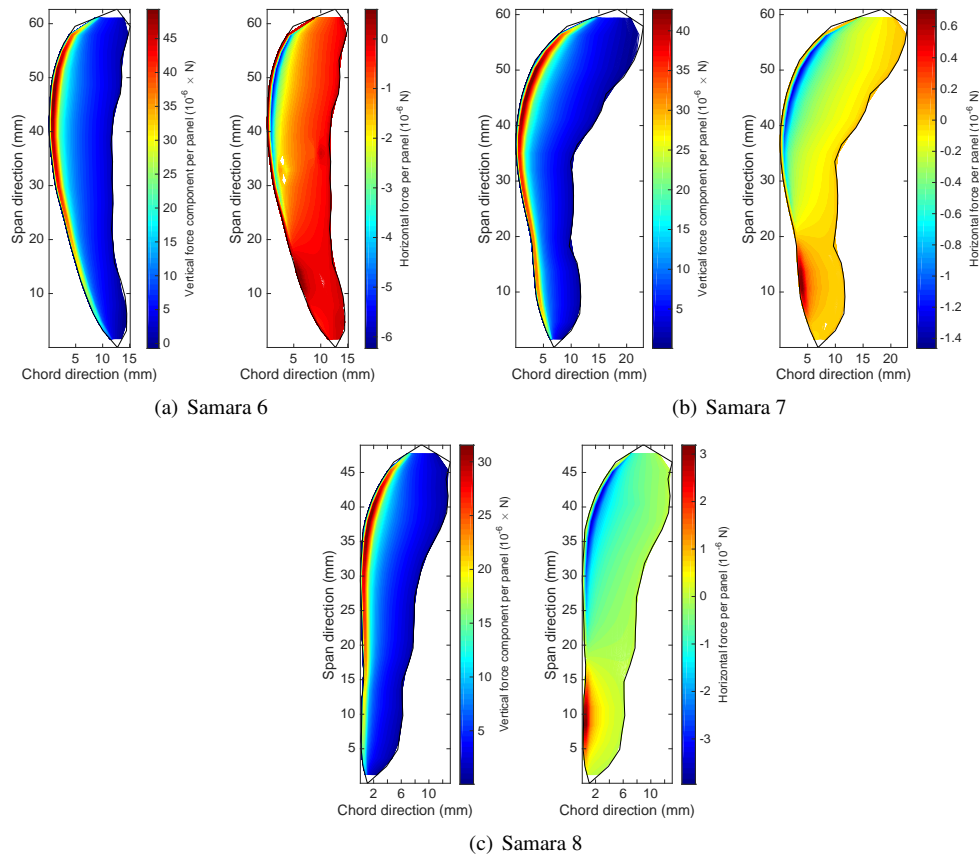
(b) Samara 7

(c) Samara 8

Figure 10. Vertical and horizontal aerodynamic forces per samara – set 2.
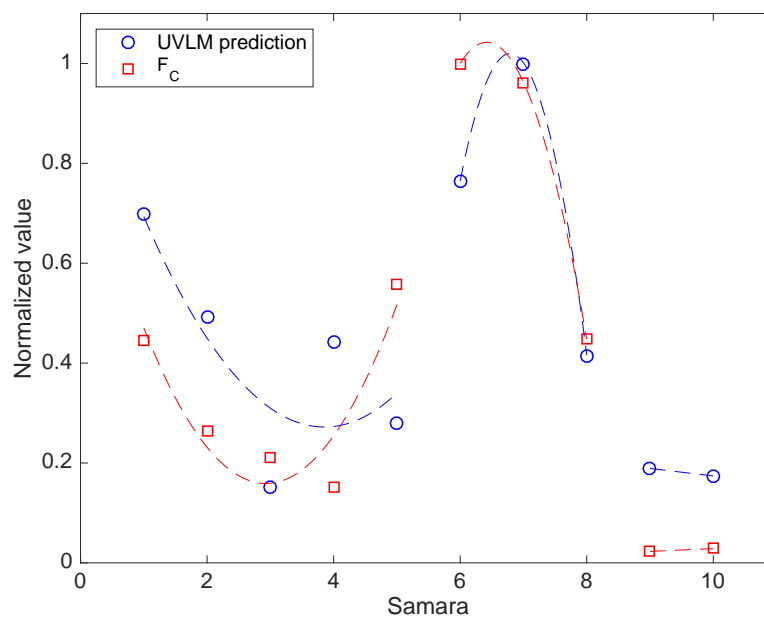

(a) Samara 9

(b) Samara 10
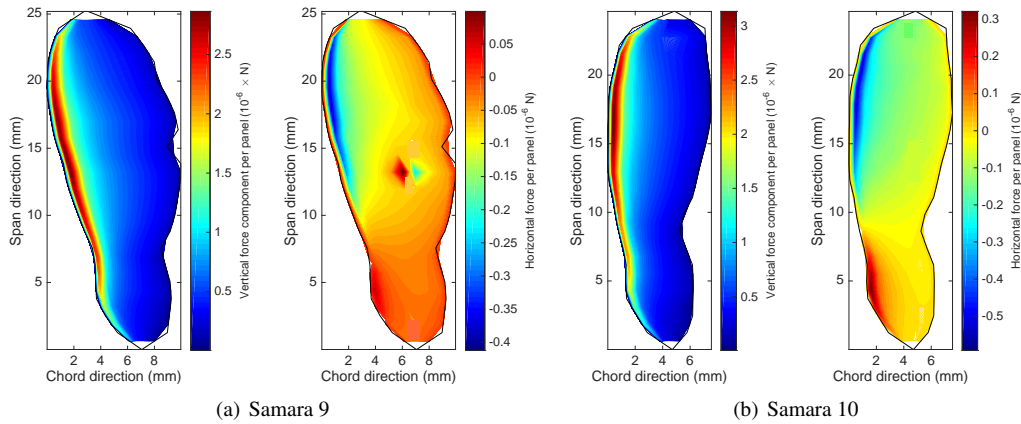
Figure 11. Vertical and horizontal aerodynamic forces per samara – set 3.

The net aerodynamic force component in the centripetal direction was also assessed from the UVLM model. Figure 12 illustrates the basic dynamics of an infinitesimal mass dm rotating at constant angular velocity ω. Therefore, the centripetal acceleration can be estimated by $\omega^2 r$, where r is the radius of the rotating path. The equivalent centripetal force can be calculated from $F_C = m\omega^2 R$.
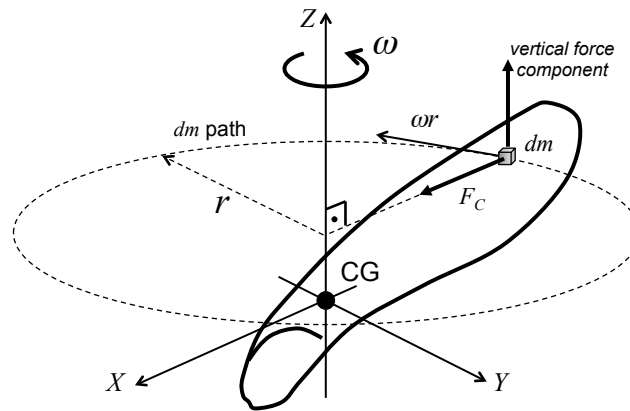
Figure 12. Forces acting on the samara rotational dynamics.

Comparing the UVLM predicted load pointing out towards the rotational axis with the centripetal force F_C in Figure 13, the results reveal that the aerodynamic model yields the same trend of variations that is determined from the calculations. The normalization values are $3.95 \times 10^{-4}N$ for UVLM prediction and $0.1186N$ for F_C.

Figure 13. UVLM predicted centripetal component compared with equivalent centripetal force obtained with experimental data – dashed lines represent trend per samara set.

In Table 5 it is compared the averaged lift coefficient obtained via the UVLM and the momentum theory. In UVLM, the lift coefficient is obtained with the average of the lift coefficient calculated for each panel, which is evaluated dividing its lift force by $1/2\rho V_K^2 \Delta S_K$, with V_K the total flow velocity at the Kth panel. It is observed that the percentage difference between the lift coefficient with respect to the momentum theory value is mostly over 20% (in absolute values). However, the momentum theory does not account for geometric aspects of the rotating body, as well as for their profile features, thereby allowing values higher than 3.0 for C_L, which is not compatible with conventional airfoil aerodynamic characteristics. Moreover, the constant 1/6 used during the lift coefficient calculation (*cf.* Eq. (12)) is not reliable, as pointed out by Azuma and Yasuda [15].

Table 5. Calculated averaged lift coefficient

Samara	Momentum theory	UVLM	Difference (%)
1	1.80	2.21	22.7
2	3.25	2.02	-37.8
3	3.85	1.58	-58.9
4	2.70	1.98	-26.7
5	1.53	1.53	0.2
6	1.03	1.32	28.6
7	1.21	1.56	28.5
8	2.21	2.66	20.2
9	2.26	1.83	-18.8
10	2.41	2.26	-6.3

6. Conclusion

This paper presented an investigation on single-winged samaras in terms of observing their falling flight until steady state constant descent speed and the application of UVLM to predict the aerodynamic loading over the samara blade. The experimental results show different regimes for the falling maple samara and corresponding descent velocity regimes. It could be observed important relations between the kinematic of the samaras and their weight. The center of mass was tracked and used to quantify the descent speed, the azimuthal rotation, and the conning angle for samaras having different aspect ratios. The aerodynamic modeling methodology was exposed to evaluate the vertical and horizontal forces in samaras using the UVLM method. Computational results show a major role for the leading edge suction in generating the unsteady forces. The samaras with straight leading edge have a better distributed force than curved leading edges samaras, where the vertical force tends to concentrate near the samara tip. Despite its linear character, the UVLM showed good simulation features to encourage its further use in the design of single-winged-like devices. Future developments comprises the use of this kind of approach to simulate the complete falling flight from rest to the steady state condition, thereby including the body dynamics to the problem.

7. References

[1] D. Lentink, A. A. Biewener, Nature-inspired flightbeyond the leap, Bioinspiration & biomimetics 5 (4) (2010) 040201.

[2] M. Y. Zakaria, H. E. Taha, M. R. Hajj, Design optimization of flapping ornithopters: The pterosaur replica in forward flight, Journal of Aircraft (2015) 1–12.

[3] D. Lentink, W. B. Dickson, J. L. van Leeuwen, M. H. Dickinson, Leading-edge vortices elevate lift of autorotating plant seeds, Science 324 (5933) (2009) 1438–1440.

[4] M. Zakaria, H. Taha, M. Hajj, Measurement and modeling of lift enhancement on plunging airfoils: A frequency response approach, Journal of Fluids and Structures 69 (2017) 187–208.

[5] R. Norberg, Autorotation, self-stability, and structure of single-winged fruits and seeds (samaras) with comparative remarks on animal flight, Biological Reviews 48 (4) (1973) 561–596.

[6] R. D. Lorenz, Spinning flight: dynamics of frisbees, boomerangs, samaras, and skipping stones, Springer, 2006.

[7] A. Kellas, The guided samara: design and development of a controllable single-bladed autorotating vehicle, Master's thesis, Massachusetts Institute of Technology (2007).

[8] W. Koenig, R. Kline, A samara-type decelerator, Tech. rep., US Army ARDC, DTIC Document – ARAED-TR-85017 (1986).

[9] P. Crimi, Analysis of samara-wing decelerator steady-state characteristics, Journal of Aircraft 25 (1) (1988) 41–47.

[10] P. Crimi, D. Jorgensen, Tests of samara-wing decelerator characteristics, in: AIAA Aerodynamic Decelerator Systems Technology Conference, 11th, San Diego, CA, 1991, pp. 265–279.

[11] P. Crimi, Finite element analysis of a samara-wing decelerator, Journal of aircraft 33 (4) (1996) 793–802.

[12] S. Valdes, I. Urza, P. Pounds, S. Singh, Samara: low-cost deployment for environmental sensing using passive autorotation, in: Robotics: Science and Systems Workshop on Robotics for Environmental Monitoring, 2012.

[13] H. Youngren, S. Jameson, B. Satterfield, Design of the SAMARAI monowing rotorcraft nano air vehicle, in: Proc. of the American Helicopter Society AHS 65th Annual Forum and Technology Display, Ft. Worth, TX, May 27-29, 2009.

[14] K. Fregene, C. L. Bolden, Dynamics and control of a biomimetic single-wing nano air vehicle, in: Proc. of the American Control Conference (ACC), Marriott Waterfront, Baltimore, MD, USA June 30-July 02, 2010, pp. 51–56.

[15] A. Azuma, K. Yasuda, Flight performance of rotary seeds, Journal of Theoretical Biology 138 (1) (1989) 23–53.

[16] C. W. McCutchen, The spinning rotation of ash and tulip tree samaras, Science 197 (4304) (1977) 691–692.

[17] R. P. Guries, E. V. Nordheim, Flight characteristics and dispersal potential of maple samaras, Forest Science 30 (2) (1984) 434–440.

[18] K. Varshney, S. Chang, Z. J. Wang, The kinematics of falling maple seeds and the initial transition to a helical motion, Nonlinearity 25 (1) (2012) C1.

[19] K. Varshney, S. Chang, Z. J. Wang, Unsteady aerodynamic forces and torques on falling parallelograms in coupled tumbling-helical motions, Physical Review E 87 (5) (2013) 053021.

[20] S. J. Lee, E. J. Lee, M. H. Sohn, Mechanism of autorotation flight of maple samaras (acer palmatum), Experiments in Fluids 55 (4) (2014) 1–9.

[21] J. F. Martiarena, V. N. Mora, J. Piechocki, Experimental study of the effect of blade curvature and aspect ratio on the performance of a rotary-wing decelerator, Aerospace Science and Technology 43 (2015) 471–477.

[22] K. Fregene, D. Sharp, C. Bolden, J. King, C. Stoneking, S. Jameson, Autonomous guidance and control of a biomimetic single-wing MAV, in: AUVSI Unmanned Systems Conference, Assoc. for Unmanned Vehicle Systems International Arlington, VA, 2011, pp. 1–12.

[23] E. R. Ulrich, D. J. Pines, J. S. Humbert, From falling to flying: the path to powered flight of a robotic samara nano air vehicle, Bioinspiration & biomimetics 5 (4) (2010) 045009.

[24] E. R. Ulrich, J. S. Humbert, D. J. Pines, Pitch and heave control of robotic samara micro air vehicles, Journal of Aircraft 47 (4) (2010) 1290–1299. doi:10.2514/1.47197.

[25] E. Limacher, D. E. Rival, On the distribution of leading-edge vortex circulation in samara-like flight, Journal of Fluid Mechanics 776 (2015) 316–333.

[26] A. Rosen, D. Seter, Vertical autorotation of a single-winged samara, Journal of applied mechanics 58 (4) (1991) 1064–1071.

[27] D. Seter, A. Rosen, Stability of the vertical autorotation of a single-winged samara, Journal of applied mechanics 59 (4) (1992) 1000–1008.

[28] D. Seter, A. Rosen, Theoretical and experimental study of axial autorotation of simple rotary decelerators, Journal of Aircraft 51 (1) (2014) 236–248.

[29] G. Matič, M. Topič, M. Jankovec, Mathematical model of a monocopter based on unsteady blade-element momentum theory, Journal of Aircraft 52 (6) (2015) 1905–1913.

[30] T. Jardin, L. David, Spanwise gradients in flow speed help stabilize leading-edge vortices on revolving wings, Physical Review E 90 (1) (2014) 013011.

[31] J. Katz, A. Plotkin, Low-speed aerodynamics, Cambridge University Press, 2001.

[32] A. Gessow, G. C. Myers, Aerodynamics of the Helicopter, Frederick Ungar, 1952.